Channel fringes in PFM1 High Resolution Interferograms

version 2.0

David Naylor, Trevor Fulton, Peter Davis

2 May 2005

Table of Contents:

1.1 Introduction

The purpose of this document is to present the first results of the analysis of the channel fringes observed in the high-resolution interferograms data taken during the SPIRE PFM1 test campaign. The location of these features is quantified, potential candidates for their cause presented, and solutions for their removal/minimization proposed.

1.2 Background

Most of the high-resolution interferograms observed during the PFM1 test campaign exhibit channel fringes – coherent signatures at increased OPDs resulting from resonant cavities within the optical path of the interferometer (Naylor *et. al.*[1]*).* Figure 1 shows an interferogram of SLW observed on 08 March, with the cold blackbody (T = 6K) as a source in one port the SPIRE FTS and the interior of the cryostat (SCAL switched off) in the other port. Note the dominant feature present from about 9 to 11 cm OPD for SLW. It is this feature that is the subject of this note.

[1] D. A. Naylor, A. A. Schultz and T. A. Clark, "Eliminating channel spectra in Fourier transform spectroscopy", Appl. Opt., **27**, 2603 (1988)

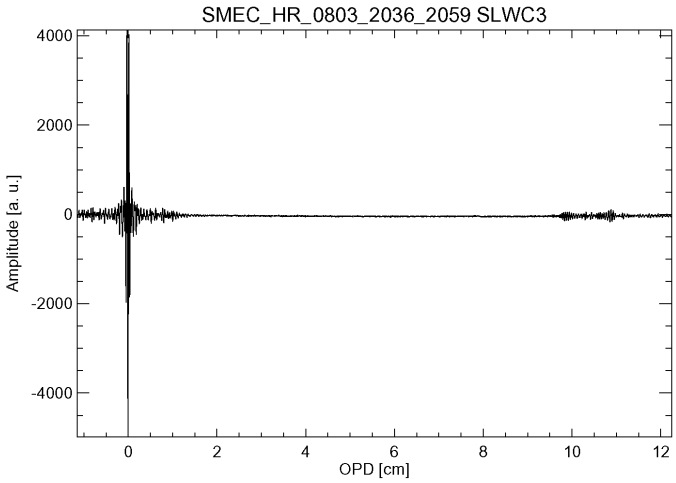

Figure 1: Typical high-resolution SLW interferogram observed during the SPIRE PFM1 test campaign

Figure 2 shows the same interferogram, but with two regions highlighted. The region coloured green is a 1024-point window centred at the zero path difference position. The region highlighted in red is a 1024-point window of the channel fringe.

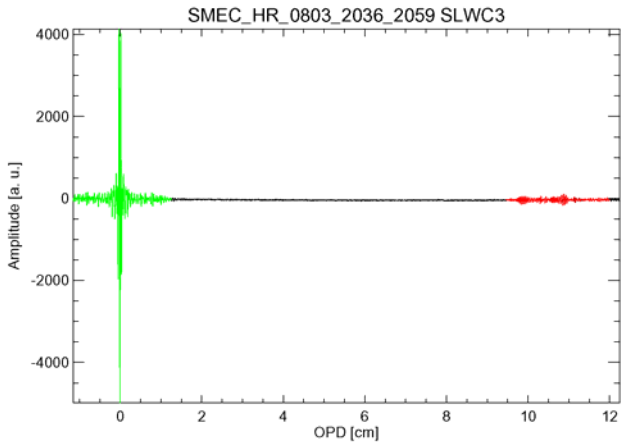

Figure 2: SPIRE PFM1 SLW interferogram. The green portion is the region about zero path difference, the red portion is a region containing the channel fringe.

Figures 3 and 4 show the power spectra for the green and red regions of the interferogram. The first figure shows the entire spectrum up to the Nyquist frequency, while the second figure shows only that portion of the spectrum within the SLW band. Note that in each of these figures the power spectrum for the red region has been scaled so that its maximum agrees with the maximum of the power spectrum of the green region.

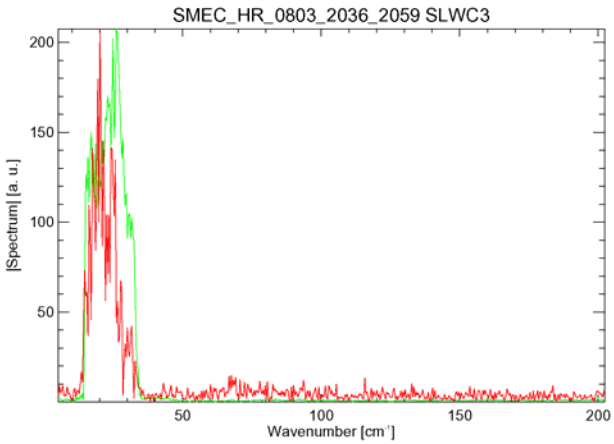

Figure 3: SPIRE PFM1 SLW spectrum. The green curve is the power spectrum from the ZPD portion of the interferogram, the red curve is the power spectrum from that portion of the interferogram containing the channel fringe. The red curve has been scaled to match the green curve.

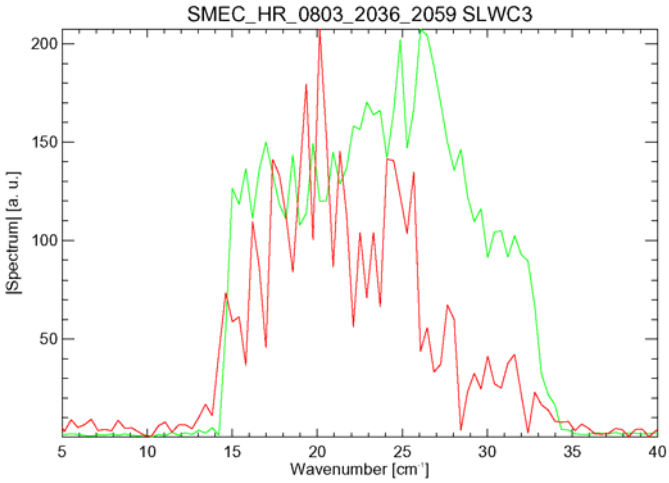

Figure 4: Expanded region of Figure 3.

Figure 4 clearly shows that the channel fringe contains essentially the same spectral components as those derived from the ZPD information.

The above analysis was undertaken for all of the pixels in both the SLW and SSW arrays for all of the cold blackbody observations taken on 08 March 2005. The figures that follow show some sample interferograms for all of the SLW and SSW pixels for the 11K and 13K cold blackbody observations. For each plot, only that portion of the interferogram that contains the channel fringe is shown. The channel fringe is present in most of the detector pixels in both arrays, the

notable exceptions being SSWD5, SSWD7, SSWF4, SSWG3, and SSWG4 pixels on which very little signal was observed.

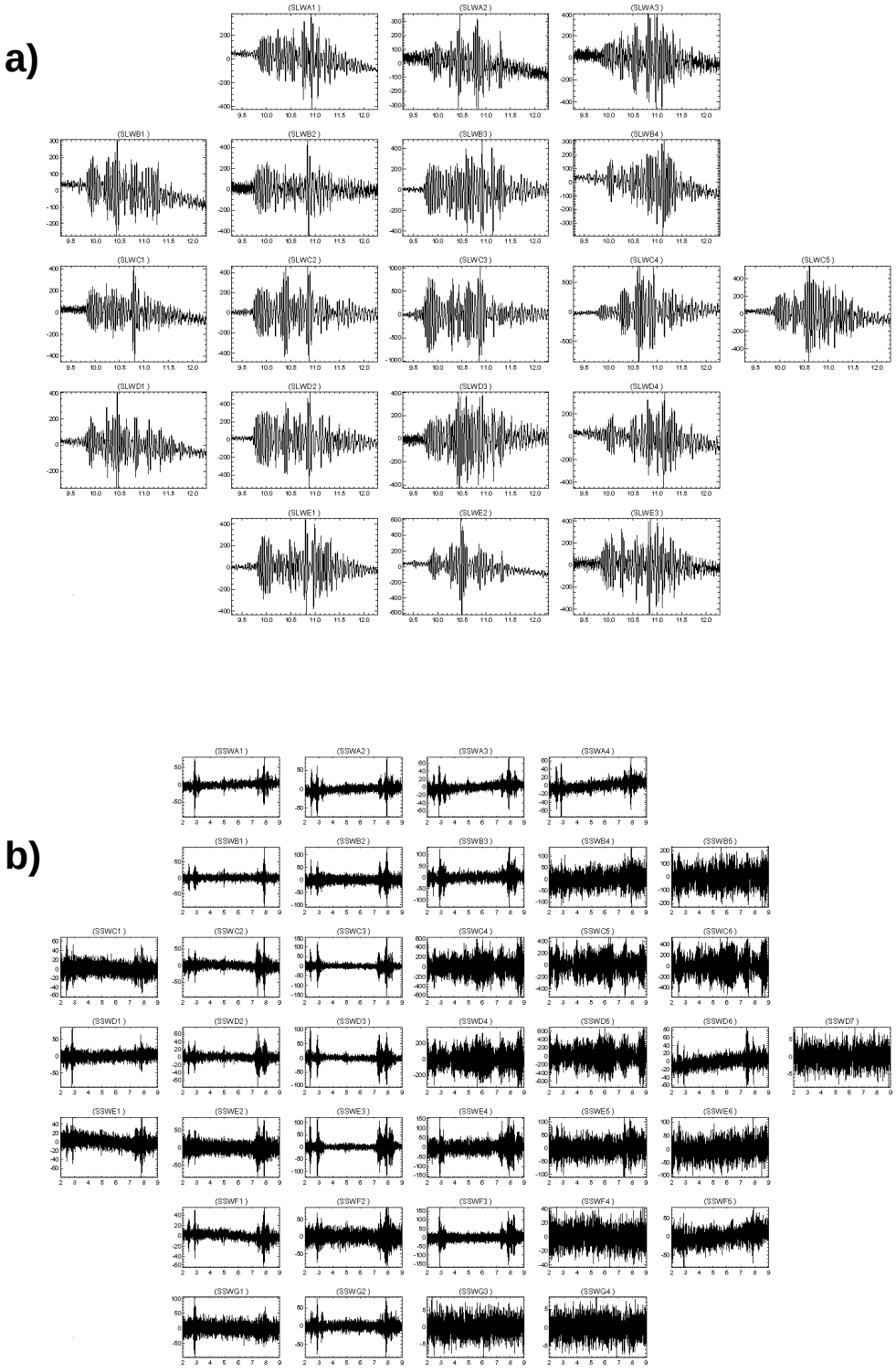

Figure 5: Observed channel fringes: a) SLW (labelled range 9.8 – 12 cm OPD), b) SSW (labelled range 2 – 9 cm OPD)

Figures 6-9 show a more detailed analysis of the channel fringes for two pixels in each array when the cold blackbody was set to 11K. The pixels featured are SLWA1, SLWC3, SSWA2, and SSWD3. In each figure, a sample raw interferogram is shown in the upper left plot; the corresponding baseline corrected interferogram is shown in the upper right plot. The two plots in the middle show a close-up view of the ZPD region on the left and a close-up view of the region containing the channel fringe on the right. The two plots on the bottom show the spectra for both of the interferogram regions; the black curve is the spectrum of the ZPD region while the red curve is the spectrum of the channel fringe (scaled by a factor of 10).

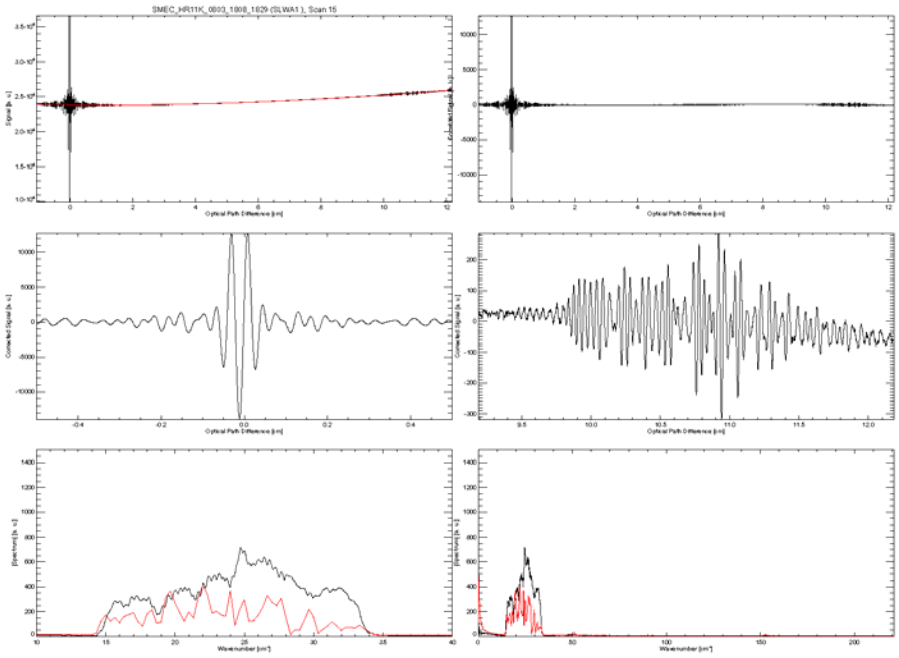

Figure 6: Channel fringe analysis: pixel SLWA1. Labelled ranges: Top 0 – 12 cm OPD; middle - 0.5 – 0.5 cm OPD and 9.8 – 12 cm respectively.

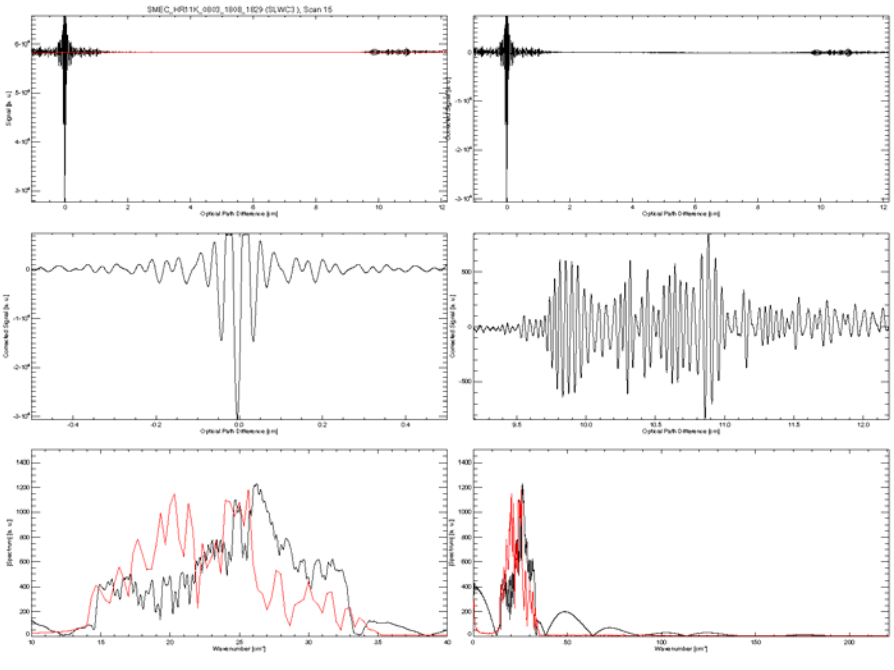

Figure 7: Channel fringe analysis: pixel SLWC3. Labelled ranges: Top 0 – 12 cm OPD; middle - 0.5 – 0.5 cm OPD and 9.8 – 12 cm respectively.

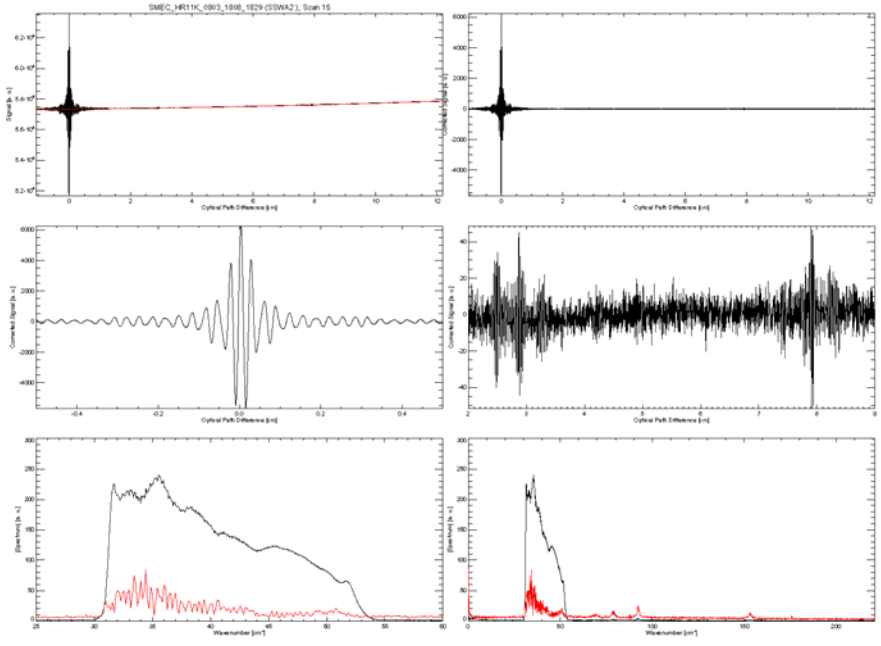

Figure 8: Channel fringe analysis: pixel SSWA2. Labelled ranges: Top 0 – 12 cm OPD; middle - 0.5 – 0.5 cm OPD and 2 – 9 cm respectively.

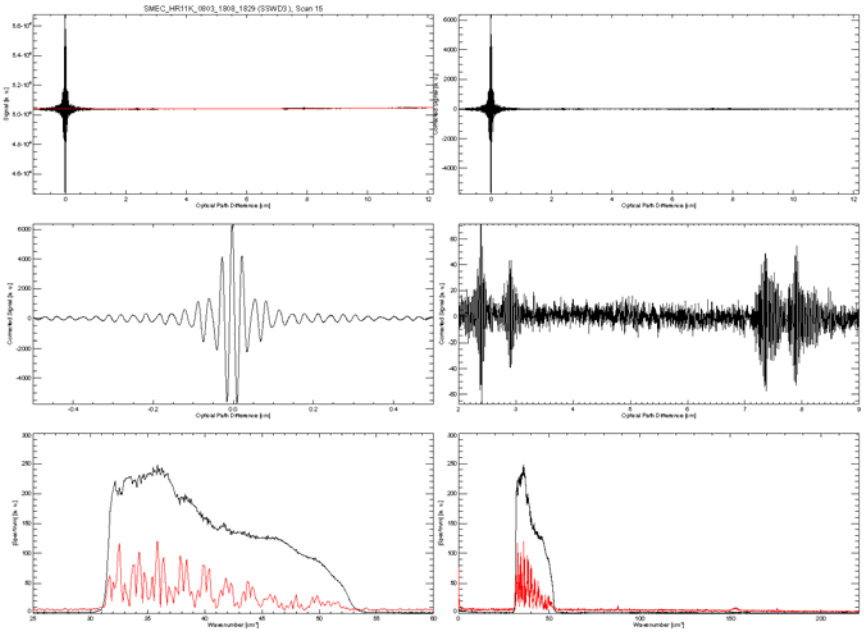

Figure 9: Channel fringe analysis: pixel SSWD3 Labelled ranges: Top 0 – 12 cm OPD; middle - 0.5 – 0.5 cm OPD and 2 – 9 cm respectively.

Figures 6–9 show that channel fringes appear on both the central pixels (SLWC3 and SSWD3) as well as the outer pixels (SLWA1 and SSWA2). Moreover, as observed previously, the spectral content of the channel fringe contains essentially the same spectral components as those derived from the ZPD information. Moreover, while the location of the channel fringes are similar for pixels of the same array, there is a marked difference in the location of the features between the two detector arrays.

1.3 Quantitative Analysis

An analysis was undertaken in order to determine the location of the channel fringes observed in the high-resolution interferograms. Although the location of the fringes is similar from one pixel to another of the same array, their shape changes which makes it difficult to pinpoint the exact location of the feature. In light of this, it was decided to concentrate in this preliminary analysis on two aspects of the channel fringes; the location of the onset of the fringe and the location of the maximum deviation from the baseline within the fringe. These two positions were found for all of the pixels in each array. The procedure employed to determine these position is described below:

1. The recorded detector signals were interpolated onto an evenly spaced position grid (using the interpolated SMEC positions) to create an interferogram.
2. The interferograms were then divided into sub-regions according to the presence of the channel fringe. For the SLW array the sub-region was from 9cm to 13cm OPD. For the SSW array, two sub-regions were used; the first was from 1.8cm to 4.0cm OPD, the second was of the range between 6.6cm and 8.6cm OPD.
3. In order to increase the signal to noise ratio of the interferograms, a series of interferograms were averaged together. Due to the inherent asymmetries between the forward and reverse interferograms forward and reverse scans were averaged independently.
4. Within each of the subsections, the position where the maximum deviation from the baseline signal was recorded. To determine the position where the signal first starts to deviate from the baseline, the so-called onset of the fringe, a threshold equal to a fraction of the maximum deviation within the region of interest was used. The onset positions were calculated for a series of fractional values and then averaged together (the range of fractional values used for the determination of the onset of the fringing were 20%, 25%, 30%, 35%, 40%, 45%, and 50%.)

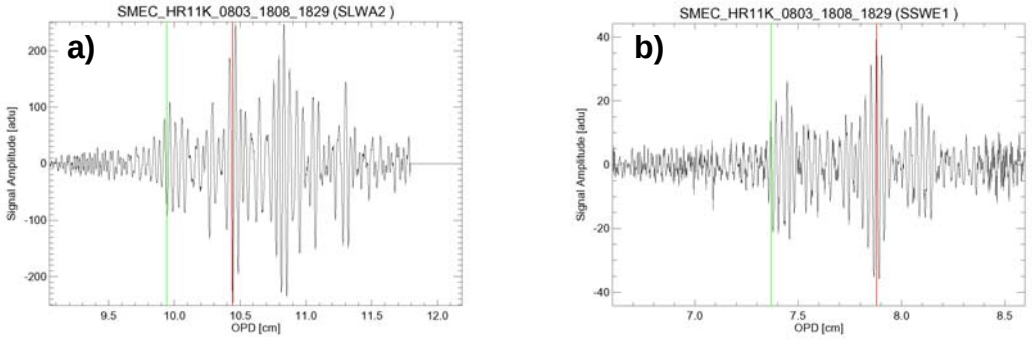

Figure 10: Channel fringe regions a) SLW, b) SSW. The green lines show the positions of the onset of the fringe feature, the red lines show the positions of maximum deviation within the feature region. For these figures, a threshold of 35% of the maximum deviation was used to determine the onset of the channel fringe.

Based on the above criteria, the positions of the onset and the maximum deviation for the recognizable channel fringes were determined and are shown in the following tables. Note that the entries in red denote those pixels in the SSW array that were observed to have higher noise levels.

Pixel	A	B	C	D	E
1	10.014 ± 0.158	9.876 ± 0.033	9.968 ± 0.171	9.885 ± 0.021	9.872 ± 0.027
2	10.032 ± 0.179	9.878 ± 0.280	9.872 ± 0.201	9.800 ± 0.046	10.082 ± 0.212
3	10.162 ± 0.164	9.833 ± 0.125	9.754 ± 0.020	9.920 ± 0.186	9.925 ± 0.057
4		10.217 ± 0.321	10.312 ± 0.109	10.188 ± 0.281	
5			10.134 ± 0.230		

Table 1: Channel fringe onset locations (cm OPD) for the SLW array, CBB temperature = 11K

Pixel	A	B	C	D	E	F	G
1	2.765 ± 0.228	2.271 ± 0.206	2.134 ± 0.293	2.519 ± 0.286	2.082 ± 0.282	2.287 ± 0.236	2.450 ± 0.499
2	2.296 ± 0.249	2.139 ± 0.288	1.965 ± 0.186	2.116 ± 0.246	1.868 ± 0.102	2.224 ± 0.475	2.410 ± 0.283
3	2.272 ± 0.277	2.239 ± 0.264	2.285 ± 0.206	2.304 ± 0.076	2.332 ± 0.030	2.763 ± 0.274	1.805 ± 0.005
4	2.453 ± 0.084	1.863 ± 0.145	1.808 ± 0.008	1.850 ± 0.150	2.270 ± 0.277	1.827 ± 0.025	1.805 ± 0.008
5		1.818 ± 0.022	1.806 ± 0.006	1.806 ± 0.005	1.893 ± 0.186	2.099 ± 0.357	
6			1.807 ± 0.009	2.026 ± 0.201	1.810 ± 0.012		
7				1.808 ± 0.011			

Table 2: Channel fringe onset locations (cm OPD) for the SSW array, Region = 1.8cm - 4.0cm, CBB temperature = 11K

Pixel	A	B	C	D	E	F	G
1	7.362 ± 0.124	7.707 ± 0.240	7.126 ± 0.299	7.065 ± 0.261	7.259 ± 0.201	7.322 ± 0.203	6.918 ± 0.334
2	7.462 ± 0.231	7.367 ± 0.031	7.286 ± 0.065	7.248 ± 0.092	7.239 ± 0.123	7.093 ± 0.355	7.544 ± 0.250
3	7.477 ± 0.173	7.702 ± 0.178	7.403 ± 0.217	7.221 ± 0.031	7.266 ± 0.043	7.467 ± 0.187	6.617 ± 0.027
4	7.329 ± 0.370	7.088 ± 0.362	6.694 ± 0.204	6.632 ± 0.021	7.183 ± 0.210	6.601 ± 0.000	6.607 ± 0.007
5		6.601 ± 0.000	6.609 ± 0.005	6.610 ± 0.005	6.994 ± 0.370	6.817 ± 0.291	
6			6.610 ± 0.006	7.264 ± 0.235	6.602 ± 0.001		
7				6.607 ± 0.012			

Table 3: Channel fringe onset locations (cm OPD) for the SSW array, Region = 6.6cm - 8.6cm, CBB temperature = 11K

Pixel	A	B	C	D	E
1	10.946	10.458	10.806	10.459	10.809
2	10.450	10.864	10.880	10.885	10.510
3	10.978	10.925	10.865	10.455	10.848
4		11.124	10.628	11.134	
5			10.600		

Table 4: Positions of maximum deviation (cm OPD) for the SLW array, CBB temperature = 11K

Pixel	A	B	C	D	E	F	G
1	2.878	2.473	2.459	2.847	2.879	2.896	2.865
2	2.877	2.908	2.912	2.886	2.662	2.903	2.896
3	2.881	2.908	2.922	2.396	2.395	2.912	2.423
4	2.877	2.875	2.840	2.395	2.931	2.195	2.802
5		2.379	2.606	2.385	2.930	2.865	
6			2.378	2.463	2.475		
7				2.744			

Table 5: Positions of maximum deviation (cm OPD) for the SSW array, Region = 1.8cm - 4.0cm, CBB temperature = 11K

Pixel	A	B	C	D	E	F	G
1	7.902	7.903	7.884	7.817	7.881	7.902	7.906
2	7.924	7.929	7.897	7.421	7.874	7.889	7.865
3	7.915	7.924	7.899	7.902	7.902	7.884	7.394
4	7.897	7.934	7.937	7.942	7.888	6.895	7.141
5		7.937	7.500	8.352	7.652	7.829	
6			8.037	7.429	7.939		
7				7.622			

Table 6: Positions of maximum deviation (cm OPD) for the SSW array, Region = 6.6cm - 8.6cm, CBB temperature = 11K

1.4 Possible causes of channel fringe features

Naylor *et. al.* have shown that channel fringes like the ones observed in the SPIRE PFM1 high-resolution interferograms can be attributed to a resonant cavity located in, and normal to, the parallel output beam. The channel fringes appear at positions of optical path difference, Δ, given by

$$\Delta = \pm 2mnd \qquad (m = 1,2,3,\ldots,\infty) \qquad \textbf{(1)}$$

where n is the refractive index of the sample and d is the cavity thickness at normal incidence.

The optical layout of SPIRE shows that while there are no cavities in the output beam that are plane-parallel, the field lenses located at the entrance to the SLW and SSW detector assemblies have the potential to set up a resonant cavity at these long wavelengths. The field lens alone cannot be responsible for the observed features since they occur at different OPDs for the two wavebands. However, resonant cavities formed with the field lens do provide an explanation of the observed fringes (see Figure 11).

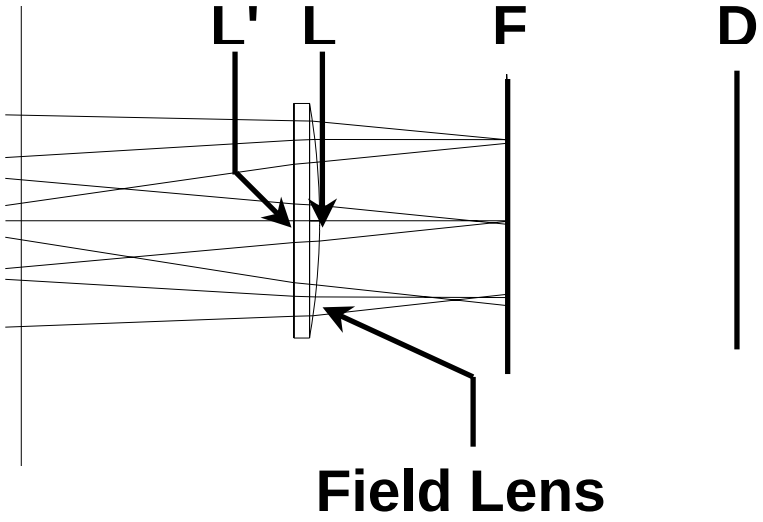

Figure 11: Spectrometer lens -- filter -- detector schematic diagram.[2]

The following tables provide a description of the labels in Figure 11 as well as the distances[3] between selected locations for each BDA.

Label	Description
L'	Flat Surface of Field Lens
L	Powered Surface of Field Lens
F	Geometrical Focal Plane (Feed horn entrance)
D	Detector Plane

Table 7: Description of labels in Figure 11.

[2] B. M. Swinyard, K. Dohlen, D. Ferand, J.-P. Baluteau, D. Pouliquen, P. Dargent, G. Michel, J. Martignac, P. Ade, P. Hargrave, M. Griffin, D. Jennings, and M. Caldwell, "The Imaging FTS for Herschel SPIRE", SPIRE-RAL-PUB-001696

[3] Hargrave, P and Tucker, C, "EIDP SPIRE - 300mK Spectrometer Filters – PFM", Issue 1.1, 28 November 2003

Description	Label	Distance [mm]	
		SLW	SSW
Powered Lens Surface to Focal Plane	LF	1.71	11.91
Flat Lens Surface to Focal Plane	L'F	3.35	13.55
Powered Lens Surface to Detector Plane	LD	48.07	35.59
Flat Lens Surface to Detector Plane	L'D	49.71	37.23

Table 8: Distances between selected points for each BDA assembly.

Table 9 shows the theoretical channel fringe locations based on the dimensions given in Table 8 and Equation 1.

Array	Reflecting Surfaces	Label	Fringe Location (cm OPD)	
			Central Pixel	Edge Pixel
SLW	Powered Lens Surface and Detector Plane	LD	9.653	9.781
	Flat Lens Surface and Detector Plane	L'D	10.169	10.096
SSW	Powered Lens Surface and Focal Plane	LF	2.382	2.510
	Flat Lens Surface and Focal Plane	L'F	2.541	2.825
SSW	Powered Lens Surface and Detector Plane	LD	7.146	7.274
	Flat Lens Surface and Detector Plane	L'D	7.304	7.589

Table 9: Expected channel fringe positions for the SLW and SSW arrays based on reflections from the field lens.

Note that for the SLW array, only the reflection between the detector plane and the field lens (L'D, LD) is considered since the theoretical location for the reflection between the focal plane and the field lens (L'F, LF) gives a theoretical fringe location very close to the ZPD position. Such a fringe is very difficult to separate from the heavily modulated signal near ZPD. Table 10 presents a comparison between the expected and observed channel fringe locations.

Array	Reflecting Surfaces		Fringe Location (cm OPD)		
			Expected	Observed	
				Onset	Maximum Deviation
SLW	Powered Lens Surface and Detector Plane	min	9.653	9.75	10.46
	Flat Lens Surface and Detector Plane	max	10.169	10.31	11.13
SSW	Powered Lens Surface and Focal Plane	min	2.382	2.03	2.46
	Flat Lens Surface and Focal Plane	max	2.825	2.76	2.92
SSW	Powered Lens Surface and Detector Plane	min	7.146	7.07	7.43
	Flat Lens Surface and Detector Plane	max	7.589	7.47	7.93

Table 10: Comparison between expected and observed channel fringe locations for the SLW and SSW arrays.

Table 10 strongly suggests that the interference arising from reflections between both surfaces of the field lens and the front and back of the detector assembly is the most likely cause of the channel fringes observed in the SPIRE PFM1 data. The fact that the fringes are not direct copies of the ZPD signal is simply due to the convex surface of the field lens that introduces a path difference variation with angle. It can be seen from Table 1 that the onset position is of the channel fringe is least for the central pixel and increases for off axis pixels as would be expected with an increasing gap in the resonant cavity. It is somewhat surprising that the most intense fringe appears to be due to a reflection from the plane of the detectors and not the focal plane.

1.5 Possible remedies

Since there would appear to be compelling evidence for the field lenses being the principle source of the channel fringes possible remedies include:

1. Remove the field lenses and live with the non-telecentricity of the beam. (Filter may still set up a resonant cavity)
2. Use lower refractive index lenses or better still coat the lenses with antireflection (ar) coating (on both surfaces). Peter Ade's group has made significant advances in this area in recent years and this will certainly help.

3. Reverse (ar-coated) lens orientation – this would give greater fringe amplitude (more parallel cavity) but less cross talk (from radiation entering neighbouring horns). Our experience (Naylor *et al*.) has been that it is easier to correct for a channel fringe formed by a parallel cavity. (The devil you know being better than the one you don't!)
4. Redesign/rebuild detector feedhorn assembly to have spherical integrating cavities – clearly an unacceptable option.

If the analysis is correct, it is somewhat surprising that significant energy is returned from the detector block to the field lens where, having reflected off the convex surface, it can enter an adjacent feedhorn. Cross talk is one aspect of the PFM1 tests that is difficult to measure but must surely be occurring. Unfortunately the fact that one end of the cavity has a convex surface makes it very difficult to estimate the absolute magnitude of the channel fringe.

Note: while it may seem that a simple solution would be to measure interferograms out to OPDs just less than the location of the channel fringe, one must remember, however, that this is a coherent pattern with information contained at all OPDs. Moreover, since there will be no simple relation between the phase of the ZPD region and that of the channel fringe, detailed phase correction will prove difficult – especially in the case of SLW where, if the analysis is correct, a channel fringe must exist close to the ZPD region.

Intensity of channel fringes in SPIRE PFM1 interferograms as a function of CBB temperature

1.6 Introduction

Channel fringes have been observed in the high-resolution interferograms recorded during the SPIRE PFM1 test campaign. A prior analysis[4] focussed on the location of these channel fringes (in terms of OPD) and to a lesser extent on the spectral content of the channel fringes. The analysis presented in this document is an attempt to determine if a relationship exists between the amplitude of the observed channel fringes and the intensity of the input source of the spectrometer.

1.7 Background

Most of the high-resolution interferograms observed during the PFM1 test campaign exhibit channel fringes – coherent signatures at increased optical path differences (OPDs) resulting from resonant cavities within the optical path of the interferometer (Naylor *et. al.*[5]*).* The plots shown in Figure 12 are sample interferograms for the pixel C3 in the SLW (a) and SSW (b) array observed on 08

[4] D. Naylor *et. al.*, "*Channel Fringes in PFM1 High Resolution Interferograms*", 11 April 2005
[5] D. A. Naylor, A. A. Schultz and T. A. Clark, "Eliminating channel spectra in Fourier transform spectroscopy", Appl. Opt., **27**, 2603 (1988)

March 2005. For the plots in Figure 12, the cold blackbody (T = 9.5 K) was the source in one port of the SPIRE spectrometer and the interior of the cryostat (T = ~4.5 K, SCAL switched off) in the other port. The features in the highlighted regions are the observed channel fringes.

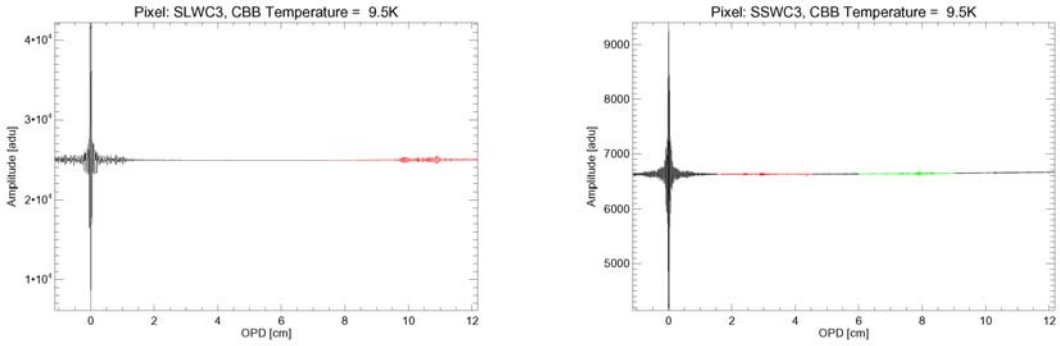

Figure 12 Sample PFM1 Interferograms. (**a**) SLW array, pixel C3; (**b**) SSW array, pixel C3.

The current objective is to determine if the amplitude of the observed channel fringes is correlated to the difference between the fluxes at the two input ports of the spectrometer. The analysis focused on a subset of the PFM1 data for which high-resolution interferograms were available. One port of the FTS viewed the interior of the cryostat, the other port viewed the cold blackbody (CBB) which was operated at four different temperatures. The data analyzed are listed in Table 11.

Scan Time[hh:mm:ss] UTC		Scan Limits [mm]			Iterations	Input ports
Start	End	Start	End	Distance		
20:38:00	20:59:00	4.86	39.26	34.40	16	CBB @ 6.5 K
17:34:00	17:54:00	4.88	39.00	34.12	16	CBB @ 9.5 K
18:09:00	18:36:00	4.86	39.26	34.40	16	CBB @ 11.5 K
19:46:00	19:56:00	4.86	39.26	34.40	4	CBB @ 13 K

Table 11: SPIRE PFM1 Datasets used for this analysis. Each data set was recorded on 08 March 2005. For each data set, the second spectrometer input port was the interior of the cryostat (T ~4.5 K).

1.8 Analysis

The method used to study the relation between channel fringe intensity and the difference between the source input intensity is described below:

5. The recorded detector signals were first interpolated onto evenly spaced position grids (using the interpolated SMEC positions) to create an interferogram.
6. For each set of scans at a given CBB temperature, an average was computed in order to increase the signal-to-noise ratio.

7. Using the previously determined locations of the channel fringes, short fixed regions about their centres were Fourier transformed to the spectral domain. The regions chosen for this analysis are listed in Table 12.

Channel Fringe	Approximate Fringe Centre OPD [cm]	Region of Interest OPD [cm]
SLW1	10	7.5 —12.5
SSW1	2.75	1.5 — 4.5
SSW2	7.75	6.5 — 9.5

Table 12: Channel Fringe Regions.

8. The absolute spectral intensity for each channel fringe region was integrated over the observed band edges[6], shown in Table 13.

Optical Band	Integration Limits [cm^{-1}]
SLW	14 — 34
SSW	30 — 54

Table 13: Limits of Integration for each Optical Band

9. Finally, the expected integrated spectral intensity, for each band, corresponding to the difference in temperature of the two input ports of the FTS, was calculated for each CBB temperature setting as shown in Fig. 2.

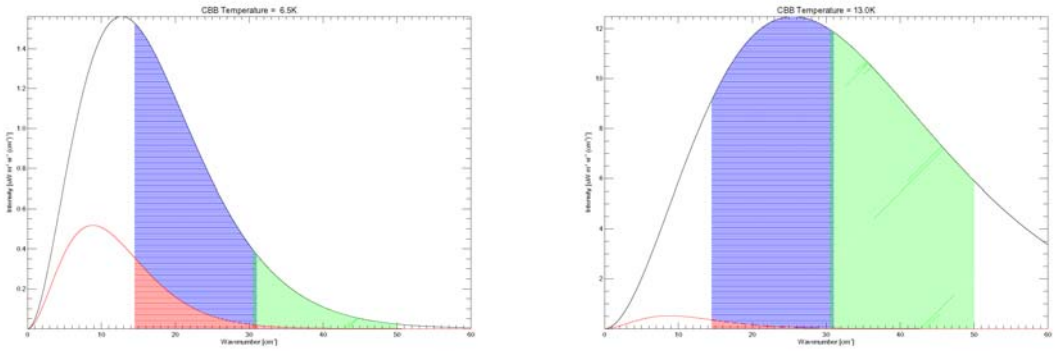

Figure 13: Expected Spectral Intensity. (**a**) CBB temperature = 6.5K, (**b**) CBB temperature = 13K. The black curve in each figure is the Planck curve for the CBB, the red curve is the Planck distribution for the second input port which viewed the interior of the cryostat (T ~4.5 K). The area of the solid region represents the expected integrated spectral intensity for SLW (**blue**) and SSW (**green**).

Thesis: If the measured channel fringe intensity is directly related to the difference between the intensities of the two input ports of the FTS, one would

[6] T. Fulton and P. Davis, "*PFM1 SMEC Scan Results*", 23 March 2005

expect a plot of the measured intensity (step 4) versus the expected intensity (step 5) to be a straight line.

1.9 Caveats

1. Although the ZPD region of some interferograms is saturated, by using the channel fringes, with their reduced amplitude, we are less vulnerable to saturation and non-linear effects; these effects have been neglected.
2. It is assumed that the gains and offsets for each pixel are constant during the four CBB temperature measurements.
3. The forward and reverse interferogram scans were averaged separately and then Fourier transformed. The integrated spectral intensity for the forward and reverse scans was computed and averaged to give one value for each pixel at each CBB temperature.

1.10 Results and Discussion

1.10.1 Measured versus Expected Channel Fringe Intensity

Figure 14and Figure 15 show plots of the measured integrated spectral intensity (y axis) versus the expected integrated spectral intensity (x axis) for the data sets listed in Table 11.

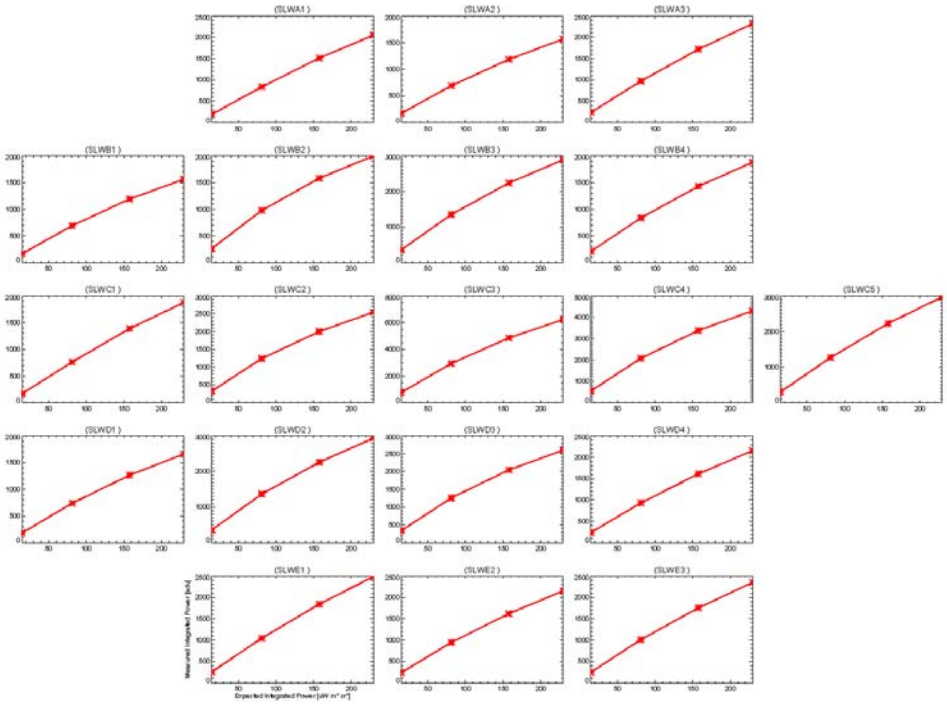

Figure 14: Integrated Spectral Intensity, measured vs. expected, SLW array. The integrated spectral intensity as calculated from the channel fringe

spectra compared with the integrated spectral intensity for the difference between two theoretical blackbodies.

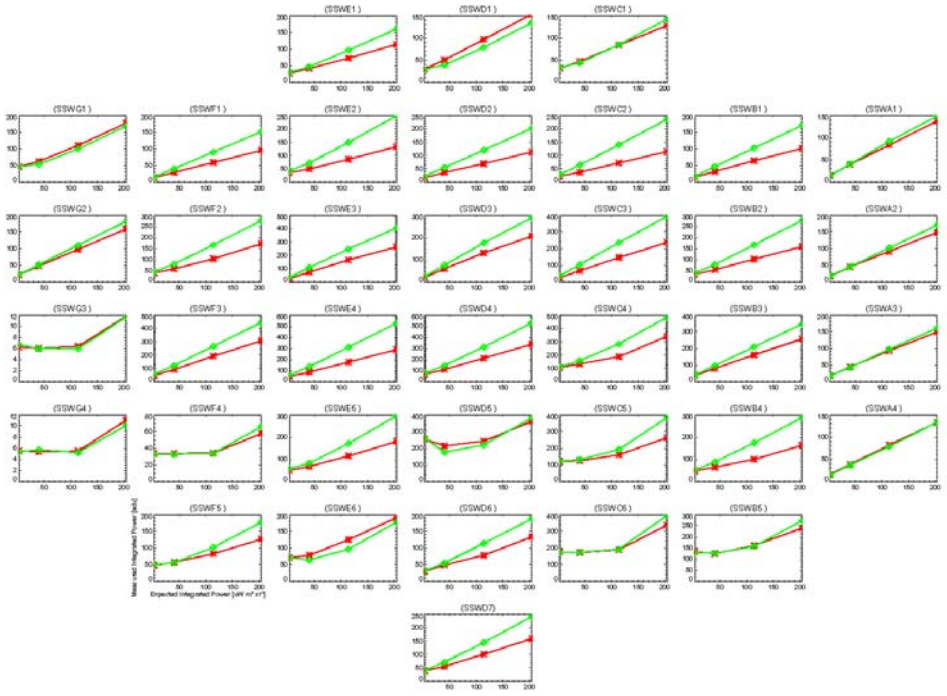

Figure 15: Integrated Spectral Intensity, measured vs. expected, SSW array. The integrated spectral intensity as calculated from the channel fringe spectra compared with the integrated spectral intensity for the difference between two theoretical blackbodies. The **red** curves represent the channel fringe region near 2.75cm OPD (SSW1); the **green** curves represent the channel fringe region near 7.75cm OPD (SSW2).

Figures 3 and 4 show that the integrated spectral intensity increases monotonically with the temperature of the CBB. While the curves do not show a linear relationship, this is not totally unexpected since, as our earlier note showed, the spectral content of the channel fringe differs from that of the ZPD region. It is likely that this is due, in part, to the wavelength dependence of reflection/diffraction at the horn aperture, although a non-linear detector response cannot be ruled out. The SSW data have lower signal-to-noise but again the integrated spectral intensity of the two channel fringes seen in these interferograms increase with CBB temperature.

Result: The channel fringe intensity is well correlated with the CBB input intensity.

1.10.2 Spatial variation of Channel Fringe Intensity

For completeness we decided to look at how the integrated spectral intensity of the channel fringes varied across the two detector arrays. The results, shown in Fig. 5, at first glance would seem to suggest a radial dependence of the intensity of the channel fringe (for which reasonable arguments might be proposed (such as decreased efficiency of the resonant cavity for off-axis pixels)). However, this analysis implicitly assumes that each pixel has the same efficiency. Until we are able to correct for pixel-to-pixel variations (i.e. flat field) this result should be treated with caution.

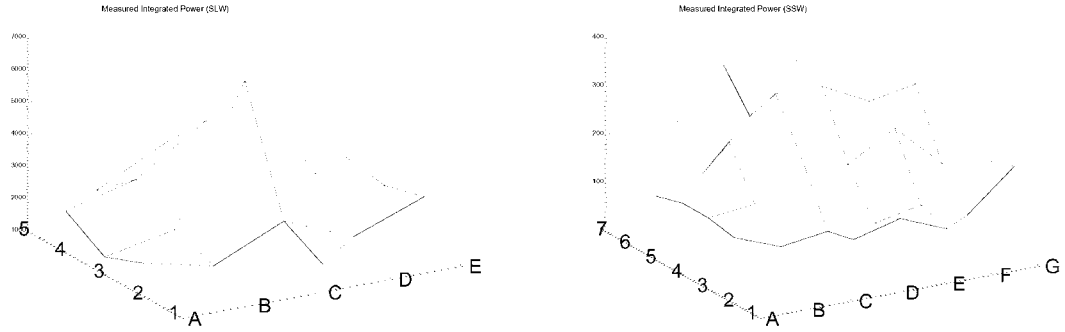

Figure 5: Measured Channel Fringe Integrated Spectral Intensity. (**a**) SLW1 channel fringe, (**b**) SSW2 channel fringe. For each plot, the temperature of the CBB was 13K.